# optica

# Spin–orbit photonic interaction engineering of Bessel beams

ARTUR ALEKSANYAN[1,2] AND ETIENNE BRASSELET[1,2,*]

[1]*University of Bordeaux, LOMA, UMR 5798, F-33400 Talence, France*
[2]*CNRS, LOMA, UMR 5798, F-33400 Talence, France*
*Corresponding author: etienne.brasselet@u-bordeaux.fr*

Interaction between the polarization and spatial degrees of freedom of a light field has become a powerful tool to tailor the amplitude and phase of light beams. This usually implies the use of space-variant photonic elements involving sophisticated fabrication technologies. Here we report on the optical spin–orbit engineering of the intensity, phase, and polarization structure of Bessel light beams using a homogeneous birefringent axicon. Various kinds of spatially modulated free-space light fields are predicted depending on the nature of the incident light field impinging on the birefringent axicon. In particular, we present the generation of bottle beam arrays, hollow beams with periodic modulation of the core size, and hollow needle beams with periodic modulation of the orbital angular momentum. An experimental attempt is also reported. The proposed structured light fields may find applications in long-distance optical manipulation endowed with self-healing features, periodic atomic waveguides, contactless handling of high aspect ratio micro-objects, and optical shearing of matter.    © 2016 Optical Society of America

*OCIS codes:* (260.1440) Birefringence; (260.6042) Singular optics; (070.3185) Invariant optical fields.

http://dx.doi.org/10.1364/OPTICA.3.000167

## 1. INTRODUCTION

Engineering the amplitude and phase of light beams is currently routinely used across various disciplines, but particularly in the field of optical manipulation [1,2]. This is usually done using spatial light modulator technology that allows almost arbitrary beam shaping in a reconfigurable manner. Technology-free options also exist, for instance, for the preparation of light beams endowed with one or several optical phase singularities. For instance, topological defects that spontaneously occur in liquid crystals have been shown to behave as efficient and reconfigurable singular phase masks for the generation of single or an array of optical vortices [3]. Tailored technology-free spin–orbit photonic interaction engineering (SOPHIE) can also be achieved by using homogeneous optically anisotropic solid crystals, as earlier shown in [4–6] for diffracting beams and in [7,8] for nondiffracting beams; see [9] for a review.

Here we propose to use SOPHIE to impart various kinds of periodic modulation of the spatial distribution of intensity, phase, and polarization to nondiffracting Bessel-like beams propagating in free space. As such, these results go beyond the previously discussed SOPHIE of paraxial [8] and nonparaxial [10] Bessel beams that lead to spatially modulated Bessel beams in uniaxial dielectric media. This is made possible by using an axicon carved in a uniaxial crystal. Its SOPHIE capabilities are theoretically outlined within the paraxial approximation, hence assuming flat enough axicons. Various incident fields impinging on the tip of the birefringent axicon are considered: circularly polarized Gaussian beams, incoherent superposition of contracircularly polarized Gaussian beams, and circularly polarized Laguerre–Gaussian beams, for which SOPHIE leads to distinct classes of spatially modulated fields. Then we report on experimental observations and discuss possible application potential for the optical manipulation of atoms, micro-objects, and soft matter.

## 2. GENERAL FRAMEWORK

### A. Transverse-to-Longitudinal Structuring

An option to realize free-space spatial modulation of Bessel beams along the propagation direction is to interfere two copropagating or contrapropagating coherent Bessel beams. In the former case, periodic intensity modulation is obtained when the individual propagation constants differ [11]. On the other hand, the two beams can also have identical propagation constant magnitude when they travel in opposite directions [12]. It is also possible to use a single beam focused by an (isotropic) axicon provided that the incident beam is endowed by transverse spatial modulation, say with period $\Lambda$. Indeed, transverse modulation is mapped into longitudinal modulation with period $\Lambda/\tan\gamma$ ($\gamma$ is the external geometrical tilt angle at the output of the axicon; see Fig. 1) along the line of focus of the axicon. Such a transverse-to-longitudinal structuring strategy has been realized by using higher-order radial Laguerre–Gaussian incident beams [13]. However, the longitudinal modulation obtained is limited to intensity modulation, is only approximately periodic, and has a limited number

Corrected 5 February 2016
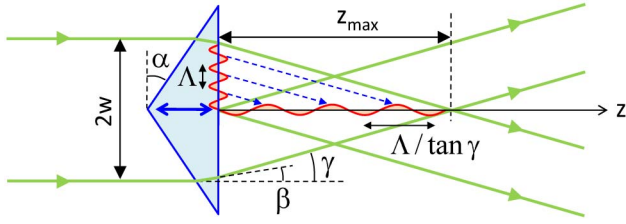
**Fig. 1.** SOPHIE geometry. An axisymmetric light beam with finite characteristic transverse size $w$ impinges on a birefringent axicon, defined by the angle $\alpha$, carved in a uniaxial crystal whose optical axis (see double arrow) lies along its axis of symmetry. Ray tracing for incident rays parallel to the $z$ axis at a distance $w$ from the $z$ axis allows one to define the diffraction-free characteristic distance $z_{max}$. $\beta$ refers to the geometrical internal tilt angle with respect to the optical axis, and $\gamma$ is the external angle. $\Lambda$ refers to the characteristic spatial scale associated with transverse modulation of the field at the output of the axicon that is mapped into characteristic longitudinal modulation $\Lambda/\tan\gamma$.



**Fig. 2.** Notations used for the evaluation of the light field at a distance $z$ from the transmittance mask located at $z = 0$, near the propagation axis (in practice, up to several wavelengths from the $z$ axis). See text for details.

of oscillations directly governed by the radial index $p$ of the Laguerre–Gauss mode used.

In our case, we exploit the transverse-to-longitudinal structuring strategy mentioned above to achieve SOPHIE of Bessel beams using Laguerre–Gauss beams having $p = 0$. This is made possible when using a birefringent axicon by exploiting the anisotropy between radially and azimuthally polarized fields that are polarization eigenstates for light propagating along the optical axis of a uniaxial medium [14]. Before analyzing specific capabilities offered by SOPHIE, it is useful to present a general description in the case of axisymmetric incident paraxial fields impinging at normal incidence on an axisymmetric complex transmittance mask that acts as an axicon lens (defined by external geometrical angle $\gamma$) is endowed with slowly varying amplitude along the radial coordinate (defined by characteristic length $\Lambda$).

## B. Field Description

Since Laguerre–Gauss beams form an appropriate exact complete basis of the paraxial Helmholtz equation in the cylindrical coordinate system, we consider an arbitrarily polarized incident Laguerre–Gaussian beam with radial index $p = 0$ and arbitrary azimuthal index $l$ that propagates toward $z > 0$ and impinges on the transmittance mask at $z = 0$, which also defines the beam waist location. Just before the mask, the complex representation of the incident field is written (omitting the common time factor $e^{-i\omega t}$)

$$\mathcal{E}_l(r, \varphi, z = 0^-) = E_l u_l(r/w) e^{il\varphi}(a\mathbf{c}_+ + b\mathbf{c}_-),\qquad(1)$$

where $E_l$ is a constant amplitude factor, $u_l(r/w) = (r/w)^{|l|}\exp(-r^2/w^2)$ with $w$ the beam waist radius, $(r, \varphi, z)$ are the cylindrical coordinates, and $\mathbf{c}_\pm = (\mathbf{x} \pm i\sigma\mathbf{y})/\sqrt{2}$ refers to the circular polarization basis expressed in the Cartesian unit basis $(\mathbf{x}, \mathbf{y}, \mathbf{z})$ with $|a|^2 + |b|^2 = 1$.

Then we describe the transmitted field in the Debye approximation, where the field nearby the focus of an imaging system is obtained by integrating the propagated partial plane waves that reach the focus [15]. Importantly, within this approximation, the plane wave spectrum is given by the transmitted field at $z = 0^+$. In the present case, the imaging lens is an axicon and, therefore, the partial waves of interest that reach on-axis point M are limited to those coming from the transmittance mask apodized by an
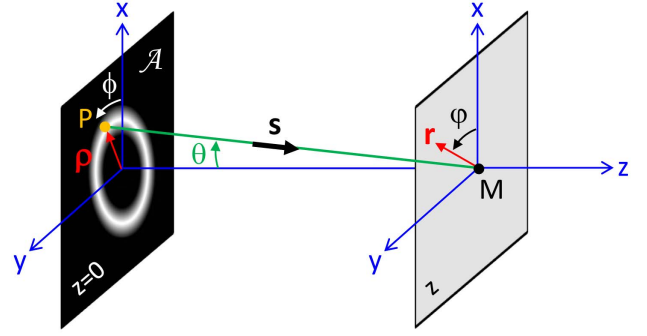
effective annular aperture ($\mathcal{A}$) with typical angular width $\delta\theta = \lambda/\Lambda$ around the angle of view $\theta = \gamma$; see the sketch in Fig. 2. Following this sketch, the field at $z$ (not too close from the mask) near the axis has the general form, up to a common phase propagation factor,

$$\mathcal{E}_l(r, \varphi, z > 0) \propto \int_{\mathcal{A}} \mathcal{E}_l'(z\tan\theta, \phi, 0^+)e^{ik\mathbf{s}\cdot\mathbf{r}}d\Omega(\theta, \phi).\qquad(2)$$

In Eq. (2) above, $\mathcal{E}_l(\rho, \phi, 0^+) = \mathcal{E}_l'(\rho, \phi, 0^+)e^{-ik\rho\tan\gamma}$, where the phase factor accounts for the focusing properties of the axicon, with $\rho$ the distance from a point P of the mask plane to the $z$ axis. In addition, $k = 2\pi/\lambda$ is the wavenumber in free space with $\lambda$ the wavelength, $\mathbf{s}$ is the unit vector pointing from P to the focus point M, $\mathbf{r}$ is the position vector in the observation plane, and $d\Omega(\theta, \phi) = \sin\theta d\theta d\phi$ is the elementary solid angle when looking at P from M; see Fig. 2.

The evaluation of the structured light field therefore requires the determination of $\mathcal{E}_l'(\rho, \phi, 0^+)$. This is done in the next subsection in the particular case of interest, when the transverse modulation results from spin–orbit interaction of light as it passes through a c-cut birefringent axicon.

## C. SOPHIE from a Birefringent Axicon

Within the paraxial approximation, the complex transmittance of the birefringent axicon is approximated by a $2 \times 2$ Jones matrix $\hat{\mathbf{T}}(\rho, \phi)$ operating on the transverse component of the incident field. Indeed, quoting Wolf and Li in [16], it is known that, when the maximum tilt angle of a partial wave is less than 30° (i.e., $\gamma < 30°$), polarization effects are not very significant in the vicinity of the focus. Such a statement has been elaborated in a previous pioneering study [17] and we will quantitatively comment on this point in Section 6. That said, one has

$$\mathcal{E}_l(\rho, \phi, 0^+) = \hat{\mathbf{T}}(\rho, \phi) \cdot \mathcal{E}_l(\rho, \phi, 0^-),\qquad(3)$$

where $\hat{\mathbf{T}}$ accounts both for the conical tilt imparted to the incident field by the axicon and the spin–orbit interaction of light as a result of different propagation constants for radially and azimuthally polarized eigenstates that are, respectively, associated with extraordinary ($n_e$) and ordinary ($n_o$) refractive indices of the uniaxial crystal. More precisely, $n_e(\beta) = n_{||}n_\perp/[n_{||}^2\cos^2\beta + n_\perp^2\sin^2\beta]^{1/2}$ for a partial wave that propagates at an angle $\beta$ from the optical axis inside the birefringent axicon (see Fig. 1), and $n_o = n_\perp$, where $n_{\perp,||}$ are the refractive indices of the uniaxial

crystal perpendicular and parallel to the optical axis. The derivation of $\hat{\mathbf{T}}$ follows from a straightforward Jones description, namely, $\hat{\mathbf{T}}(\rho, \phi) = \hat{\mathbf{R}}(-\phi)\hat{\mathbf{P}}(\rho)\hat{\mathbf{R}}(\phi)$, where $\hat{\mathbf{R}}$ is the rotation matrix and $\hat{\mathbf{P}}$ refers to the propagation in the local extraordinary/ordinary frame of the birefringent axicon. From the following expressions in the linear polarization basis $(\mathbf{x}, \mathbf{y})$,

$$\hat{\mathbf{R}}(\phi) = \begin{pmatrix} \cos\phi & \sin\phi \\ -\sin\phi & \cos\phi \end{pmatrix}, \tag{4}$$

and

$$\hat{\mathbf{P}}(\rho) = \begin{pmatrix} e^{-ik\rho(n_e(\beta)-1)\alpha} & 0 \\ 0 & e^{-ik\rho(n_\perp-1)\alpha} \end{pmatrix}, \tag{5}$$

one obtains after calculations the expression of $\hat{\mathbf{T}}$ in the circular polarization basis $(\mathbf{c}_+, \mathbf{c}_-)$:

$$\hat{\mathbf{T}}(\rho, \phi) = \exp\left(i\frac{\Delta(\rho)}{2} - ik\rho(n_\perp - 1)\alpha\right)$$
$$\times \begin{pmatrix} C(\rho) & iS(\rho)e^{-2i\phi} \\ iS(\rho)e^{2i\phi} & C(\rho) \end{pmatrix}, \tag{6}$$

with $C(\rho) = \cos[\Delta(\rho)/2]$ and $S(\rho) = \sin[\Delta(\rho)/2]$, where $\Delta(\rho)$ is evaluated to the lowest order in $\alpha$, noting that $\beta \simeq (1 - 1/n_\perp)\alpha$. This gives

$$\Delta(\rho) = [(n_\perp - 1)^2(n_\perp^2 - n_\parallel^2)/(2n_\perp n_\parallel^2)]\alpha^3 k\rho. \tag{7}$$

Remarkably, Eq. (6) is reminiscent of the description of the spin–orbit effects in a space-variant uniaxial plate endowed with a radial optical axis distribution and a birefringent phase retardation $\Delta$ that scales linearly with the distance to the propagation axis, which echoes an analogy previously discussed in [18].

Since $\gamma \simeq (n_\perp - 1)\alpha$, Eqs. (3) and (6) allow us to identify the term $\mathcal{E}'_l(\rho, \phi, 0^+)$ in Eq. (2). Indeed, noting that $|\Delta(\rho)/[k\rho(n_\perp - 1)\alpha]| \ll 1$ is always satisfied within the present paraxial framework, one gets

$$\mathcal{E}'_l(\rho, \phi, 0^+) = \begin{pmatrix} C(\rho) & iS(\rho)e^{-2i\phi} \\ iS(\rho)e^{2i\phi} & C(\rho) \end{pmatrix} \mathcal{E}_l(\rho, \phi, 0^-). \tag{8}$$

As one could expect, the $2 \times 2$ matrix in Eq. (8) corresponds to the spin–orbit transformation that describes the dynamics of optical spin–orbit coupling in uniaxial crystals [19]. Moreover, Eq. (8) allows identifying the characteristic length $\Lambda$ of transverse modulation as $\Delta(\Lambda) = 2\pi$:

$$\Lambda = \frac{2\lambda n_\perp n_\parallel^2}{(n_\perp - 1)^2(n_\perp^2 - n_\parallel^2)\alpha^3}. \tag{9}$$

### D. Field Evaluation

Integration of Eq. (2) is carried out by inserting Eq. (8) into Eq. (2). First, integration along $\phi$ is done by noting that $\mathbf{s} \cdot \mathbf{r} = -r\sin\theta\cos(\phi - \varphi)$ and exploiting the identities $\int_0^{2\pi}\exp[ix\cos(\phi - \varphi) + il\phi]d\phi = 2\pi i^l\exp(il\varphi)J_l(x)$ and $J_l(-x) = (-1)^l J_l(x)$, where $J_l$ denotes the Bessel function of the first kind of order $l$. Then, integration along $\theta$ is performed, recalling that slowly varying transverse modulation of the field at $z = 0^+$ implies a distribution peaked on $\theta = \gamma$ provided that $\delta\theta \ll \gamma$, hence, $\lambda/\Lambda \ll \gamma$ [condition 1]. One can thus keep only the value of the integrand at $\theta = \gamma$ provided that $kr\delta\theta \ll 1$, hence $r \ll \Lambda/(2\pi)$ [condition 2], and that $z\delta\theta \ll \Lambda$, hence $z \ll \Lambda^2/\lambda$ [condition 3]. After calculations, one gets, in the circular polarization basis,

$$\mathcal{E}_l(r, \varphi, z > 0) \propto E_l u_l(z/z_{max})e^{il\varphi}$$
$$\times \begin{pmatrix} C(\gamma z)J_l(\gamma kr) & -iS(\gamma z)J_{l-2}(\gamma kr)e^{-2i\varphi} \\ -iS(\gamma z)J_{l+2}(\gamma kr)e^{2i\varphi} & C(\gamma z)J_l(\gamma kr) \end{pmatrix}\begin{pmatrix} a \\ b \end{pmatrix}, \tag{10}$$

where $z_{max} = w/\gamma$ is the characteristic quasi-diffraction-free distance of a Bessel beam generated by a typical axicon [20].

Equation (10) emphasizes that SOPHIE leads to the transformation of an incident arbitrarily polarized Laguerre–Gaussian beam with radial order zero and azimuthal order $l$ into a coherent superposition of self-imaged beams. Namely, the output field consists of two $\mathbf{c}_+$ polarized beams endowed with Bessel features of order $l$ and $l - 2$ and two $\mathbf{c}_-$ polarized beams involving orders $l$ and $l + 2$, all of them being spatially modulated along the beam propagation.

## 3. PLANE WAVE EXCITATION

SOPHIE of Bessel beams is first illustrated in the ideal situation of a circularly polarized incident plane wave, which implies the use of Eq. (10) in the limit $w \to \infty$. The simulations are performed using wavelength $\lambda = 633$ nm and angle $\alpha = 20°$, and choosing the corresponding parameters of LiNbO$_3$, which is the uniaxial material used in experiments (see Section 5), namely, $n_\perp = 2.286$ and $n_\parallel = 2.203$, which gives $\Lambda \sim 850\lambda$. This allows us to check the three conditions for the validity of Eq. (10) given in Section 2.D. Namely, condition 1 is validated since $\lambda/\Lambda \sim 10^{-3} \ll \gamma \sim 0.45$. On the other hand, condition 2 implies observation at distance $r \ll 85$ μm from the axis, whereas condition 3 implies observation at distance $z \ll 50$ cm from the birefringent axicon, both conditions being fulfilled in Fig. 3, which shows the basic situation of a $\mathbf{c}_+$ polarized incident plane wave ($l = 0$).
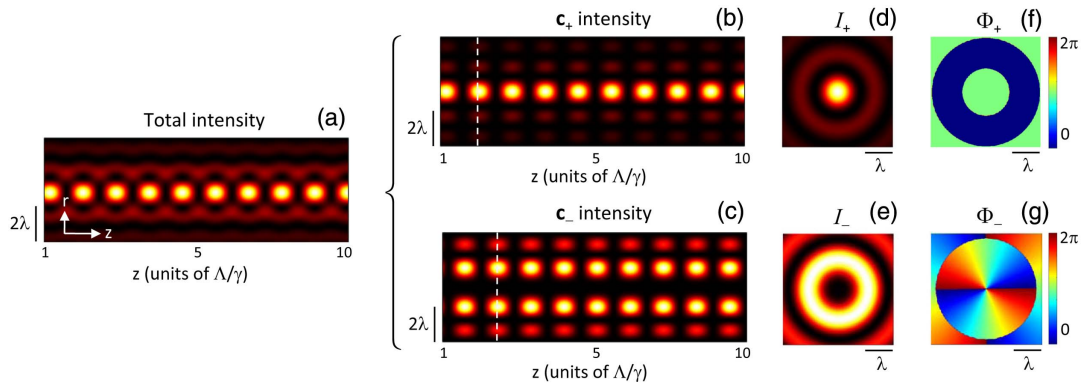
The total intensity distribution in the vicinity of the $z$ axis is shown in Fig. 3(a) over the typical range $1 < z/(\Lambda/\gamma) < 10$ that corresponds to nine self-imaging spatial periods. The normalized intensity patterns of the $\mathbf{c}_\pm$ polarized components are also shown in Figs. 3(b) and 3(c). As expected from Eq. (10), the copolarized component (here $\mathbf{c}_+$) corresponds to a fundamental Bessel beam with spatially modulated on-axis intensity, whereas the contrapolarized component (here $\mathbf{c}_-$) corresponds to a second-order Bessel beam with a spatially modulated doughnut intensity profile. This is illustrated in Figs. 3(d) and 3(e) and Figs. 3(f) and 3(g), where the transverse intensity ($I_\pm$) and phase ($\Phi_\pm$) profiles associated with local intensity maximum are shown. In particular, the characteristic on-axis optical phase singularity with topological charge 2 associated with a second-order Bessel beam is shown in Fig. 2(g). Noticeably, the sign of the latter topological charge is reversed when the helicity of the incident field is flipped, whereas the intensity patterns remain unchanged, which is a basic feature of SOPHIE.

## 4. LAGUERRE–GAUSSIAN BEAM EXCITATION

### A. General Considerations

Recalling that the above plane wave considerations represent an idealized proof-of-principle of SOPHIE of Bessel beams, a realistic approach is carried out by considering Laguerre–Gaussian incident beams [see Eq. (1)] whose finite transverse spatial extent is dictated by the beam waist radius $w$. Assuming a large enough beam waist, the characteristic length $\Lambda$ remains defined by

**Fig. 3.** (a) Total intensity distribution near the $z$ axis in the case of a $\mathbf{c}_+$ polarized incident plane wave. The intensity distribution of the $\mathbf{c}_\pm$ polarized components are shown in (b) and (c), whereas the transverse intensity ($I_\pm$) and phase ($\Phi_\pm$) profiles associated with a local intensity maximum (see dashed vertical lines) are shown in (d), (e) and (f), (g).

Eq. (9), which typically implies $w > 1$ mm. A consequence of finite beam size is that on-axis periodic intensity modulation has a Laguerre–Gaussian envelope proportional to $u_l^2(z/z_{max})$, as one can see from Eq. (10). Therefore, only a limited number $N$ of longitudinal oscillations may be of practical interest. Taking $w = 1$ cm, which is the value used in simulations, the validity of the above three conditions is thus fulfilled and one gets $N = |\Delta(w)|/(2\pi) \sim 20$.

## B. Self-Imaged Optical Bottles

Since the decomposition into circularly polarized components shown in Fig. 3 exhibits alternating bell-shaped [Fig. 3(b)] and doughnut-shaped [Fig. 3(c)] intensity profiles along the $z$ axis, this gives a basis to build up self-imaged bottle beams, i.e., an array of zeros of intensity surrounded by bright regions in three dimensions [21]. Our idea is to prepare an incident field in order that SOPHIE leads to modulated Bessel beams of order 0 and $\pm 1$ that are shifted along $z$ by half the longitudinal period $\Lambda/\gamma$.

For this purpose, there are several options. For instance, one can use an incident field that results from the incoherent superposition of two Laguerre–Gaussian beams: a $\mathbf{c}_\sigma$ ($\sigma = \pm 1$) polarized beam of order $l = 0$ and a $\mathbf{c}_{-\sigma}$ polarized beam of order $l = \sigma$. Then, by selecting the $\mathbf{c}_\sigma$ polarized component of the output field, one obtains the desired alternating sequence of bell-shaped and doughnut-shaped intensity profiles along the $z$ axis. However, the two slowly varying intensity envelopes $u_0^2$ and $u_1^2$ [see Eq. (10)], are shifted along the $z$ axis and lead to an array of optical bottles where the transverse and longitudinal "intensity caps" differ. This is summarized in Fig. 4, which shows the individual contributions of the two incident beams with identical beam waist [Figs. 4(a) and 4(b)] and their sum [Fig. 4(c)]. Still, rather isotropic optical bottles can be obtained at any desired place by adjusting the ratio between amplitudes $E_\sigma$ and $E_0$ [see Eq. (1)], as shown in Fig. 4(c). In that figure, the targeted location is $z/z_{max} \simeq 0.4$, and the corresponding ratio is $E_\sigma/E_0 \simeq 4.4$. An enlargement of the latter bottle is displayed in Fig. 4(d). Both the transverse and longitudinal intensity profiles of the bottle are shown in Figs. 4(e) and 4(f) [see dark dashed lines in Fig. 4(d)]. In addition, the isotropic character of the obtained bottle is assessed by looking at the intensity profile along the "intensity valleys" [see white dashed line in Fig. 4(d)], as shown

in Fig. 4(f). A rather good bottle is obtained, noting that the relative modulation between peak and valley intensity values around the three-dimensional dark core is $\mu = (I_{peak} - I_{valley})/I_{peak} = 0.44$.

The above limitations for obtaining a single quasi-isotropic bottle can be circumvented by using two contracircularly polarized Gaussian beams. In that case, the output intensity pattern
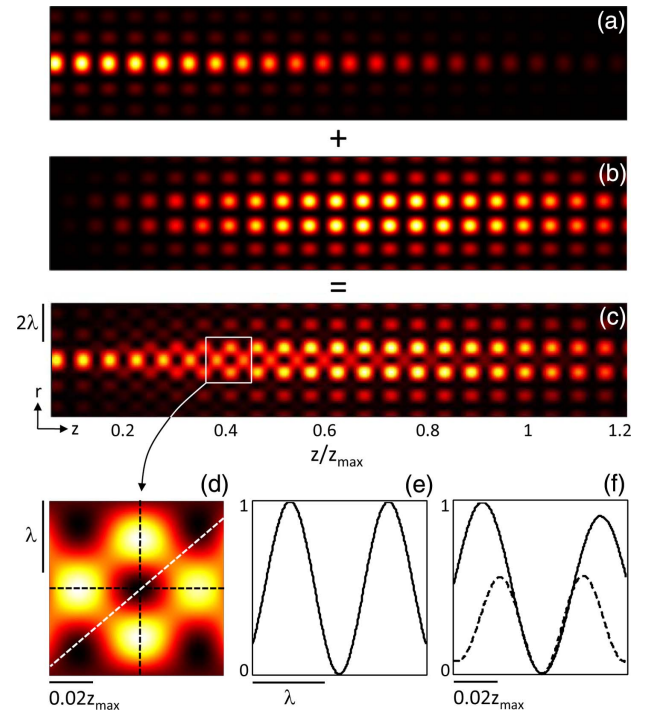


**Fig. 4.** Intensity distribution near the $z$ axis of the $\mathbf{c}_\sigma$ polarized component of the field in the case of incoherent superposition of two Laguerre–Gaussian beams: (i) a $\mathbf{c}_\sigma$ ($\sigma = \pm 1$) polarized beam of order $l = 0$ and (ii) a $\mathbf{c}_{-\sigma}$ polarized beam of order $l = \sigma$. (a) Beam (i) alone. (b) Beam (ii) alone. (c) Beams (i) and (ii) together for a ratio of amplitude $E_\sigma/E_0 \simeq 4.4$. (d) Enlargement of the region near $z/z_{max} \simeq 0.4$ that corresponds to an optical bottle. (e) Normalized transverse intensity profile; see vertical black dashed line in (d). (f) Solid curve. normalized longitudinal intensity profile [see horizontal black dashed line in (d)]; dashed curve, intensity profile along the diagonal white dashed line in (d).
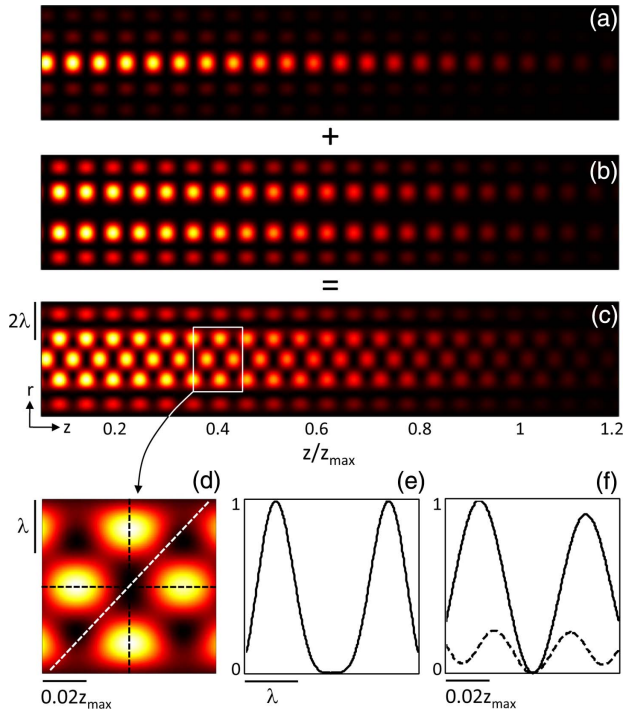
**Fig. 5.** Same as in Fig. 4 in the case of two contracircularly polarized fundamental Gaussian beams ($l = 0$) for a ratio of amplitude $\simeq 2.1$ between the $\mathbf{c}_{-\sigma}$ and $\mathbf{c}_{\sigma}$ polarized incident beams.

does not depend on the selected circular polarization state. Indeed, whatever is the handedness of the selected output circular polarization, one gets the superposition between modulated Bessel beams of order 0 and $\pm 2$ that are shifted along $z$ by half the longitudinal period $\Lambda/\gamma$. This is illustrated in Fig. 5, which is presented in a manner similar to Fig. 4 for an intensity ratio $\simeq 2.1$ between the $\mathbf{c}_{-\sigma}$ and $\mathbf{c}_{\sigma}$ polarized incident beams. However, this is at the expense of optical bottle isotropy (modulation parameter increases to $\mu = 0.76$), since the central doughnut intensity pattern of a second-order Bessel beam has a larger radius than a first-order one, as emphasized in Figs. 5(d)–5(f).

By proposing a SOPHIE approach based on a uniaxial axicon, these results contribute to previous efforts to generate free-space

single or multiple optical bottles using slabs of uniaxial [22,23] and biaxial [24,25] crystals. This may be useful for Bessel-beam-based optical trapping and manipulation of microparticles, as done from the beginning of the 2000 s in a liquid environment [12,26,27]. In particular, noting that the aspect ratio of the optical bottles obtained is typically $\Lambda/(\gamma\lambda) \sim 10^3$ with the present parameters, the proposed approach should be especially useful in the case of a single or a chain of high aspect ratio micro-objects. In particular, the photophoretic manipulation [28,29] of carbon nanotubes in gaseous media can be considered.

### C. Corrugated Optical Hollow Pipes

Exploiting the above strategy, we can also access another kind of optical field modulation along the propagation direction, namely, corrugated optical hollow pipes that correspond to self-imaged hollow beams. Among the possible options, one can use two contracircularly polarized Laguerre–Gaussian beams of order $l \neq 0$ and select the $\mathbf{c}_{-|l|/l}$ polarized component of the output field. Indeed, one obtains in that case a superposition between modulated Bessel beams of order $l$ and $l + 2\,\mathrm{sgn}(l)$ that are shifted along $z$ by half the longitudinal period $\Lambda/\gamma$. In turn, corrugated hollow pipes with increasing inner core diameter are obtained as $|l|$ increases. The results are shown in Figs. 6(a)–6(c) for $l = (1, 2, 3)$ and a ratio of amplitudes 1.33, 1.22, and 1.17 between the $\mathbf{c}_+$ and $\mathbf{c}_-$ polarized incident beams, respectively. This kind of hollow pipe equips Bessel-beam-based atomic waveguides [30] with periodic features.

### D. Self-Imaged Orbital Angular Momentum Hollow Beam

We also propose another kind of spatially modulated field that consists of quasi-nondiffracting beams with self-imaged orbital angular momentum. This is achieved by using a $\mathbf{c}_{\sigma}$ polarized Laguerre–Gaussian beam of order $l = -\sigma$, and the results in the case of $\sigma = +1$ are presented in Fig. 7. The hollow intensity map obtained is reminiscent of first-order Bessel beams; see Fig. 7(a). More precisely, the output field is the superposition of a contracircularly polarized modulated Bessel beam of order $l = \pm 1$ that is shifted along $z$ by half the longitudinal period $\Lambda/\gamma$. Therefore, the orbital angular momentum density is modulated along the $z$ axis. This is emphasized in Fig. 7(b), where the $z$-invariant intensity pattern is encoded as luminance, and the orbital angular
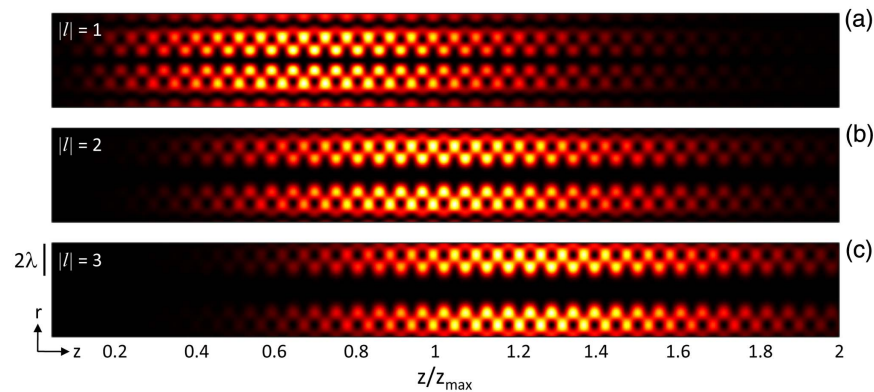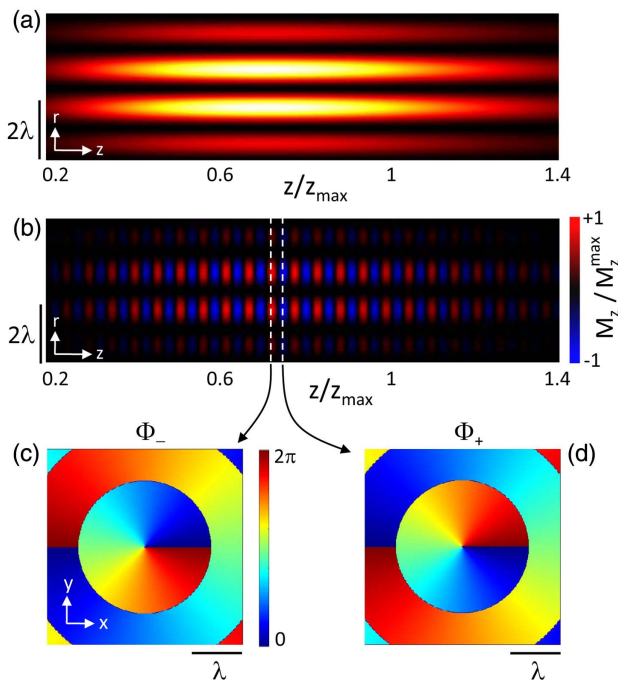


**Fig. 6.** Total intensity distribution nearby the $z$ axis of corrugated optical hollow pipes of various inner diameter obtained in the case of two contracircularly polarized Laguerre–Gaussian beams of order $l \neq 0$, by selecting the $\mathbf{c}_{-|l|/l}$ polarized component of the output field. Results are shown for $|l| = (1, 2, 3)$ for a ratio of amplitudes 1.33, 1.22, and 1.17 between the $\mathbf{c}_{-\sigma}$ and $\mathbf{c}_{\sigma}$ polarized incident beams.

momentum density $M_z$ is encoded in color scale. The latter is evaluated recalling that $M_z$ is proportional to the difference between the intensity of the beam carrying positive orbital angular momentum and that of the one carrying negative orbital angular momentum [31]. That is to say, $M_z(r, z) \propto \sigma(I_{-\sigma} - I_\sigma)$, where $I_\pm$ refers to the intensity of the $\mathbf{c}_\pm$ polarized circular component of the output field. In addition, the optical vortex skeleton of such a field is assessed in Figs. 7(c) and 7(d), which show the transverse phase profiles at two orbital angular momentum hot-spot locations.

Arguably, a practical drawback of the latter option could be its inhomogeneous polarization state. However, this issue can be circumvented by preparing an incoherent superposition of $\mathbf{c}_\sigma$ and $\mathbf{c}_{-\sigma}$ polarized Laguerre–Gaussian beams of order $l = \sigma$ with the same amplitude as the incident field. In that case, by selecting the $\mathbf{c}_\sigma$ polarized component of the output field, one gets a uniformly polarized field endowed with self-imaged orbital angular momentum. Consequently, the output polarization state can be controlled at will without affecting the orbital angular momentum content.

Noticeably, such optical fields unveil a novel application potential owing to their ability to transfer orbital angular momentum in an alternating manner along the beam propagation direction. These beams are thus capable of shearing matter, which might be useful in soft-matter viscoelastic measurements. Such "optical shearers" are another tool in completing the existing optical manipulation toolbox that already includes optical tweezers [32], optical spanners [33], optical stretchers [34], and optical twisters [35].

## 5. EXPERIMENTAL ATTEMPT

Our experimental approach is realized by using a birefringent axicon made of $LiNbO_3$ with angle $\alpha = 20°$ and a 1 in. basis diameter, with 633 nm operating wavelength, as mentioned in Section 3. Here we present results that illustrate SOPHIE in the case of an incident $\mathbf{c}_+$ polarized Gaussian beam (Fig. 3) with beam waist radius evaluated as $w \simeq 6.5$ mm. Practically, we tried to image the circularly polarized components of the field near the $z$ axis as a function of $z$ by using various microscope objectives. However, we were not able to clearly distinguish Bessel beam features, probably due to nonideal axisymmetry of the axicon itself. In fact, we recall that the fabrication of an axicon carved in $LiNbO_3$ remains a challenge itself. Therefore, instead of scanning the field along the $z$ axis, we choose to analyze the output field at the distance $z_{max}$ from the birefringent axicon [see Fig. 8(a)], which can be directly observed on a screen. By doing so, one retrieves information on SOPHIE since the $(x, y)$ observed field can be considered to be the longitudinal-to-radial projection of the field.

Experimental data are shown in Figs. 8(b) and 8(c), where Fig. 8(b) represents the intensities $I_\pm$ of the $\mathbf{c}_\pm$ polarized components, and the phase difference $\delta\Phi$ between the $\mathbf{c}_\pm$ components, respectively. The complementary periodic intensity modulation of $I_\pm$ along the radial direction is the signature of the periodic modulation shown in Figs. 3(b) and 3(c), which corresponds to the $\mathbf{c}_+$ polarized incident Gaussian beam. On the other hand,
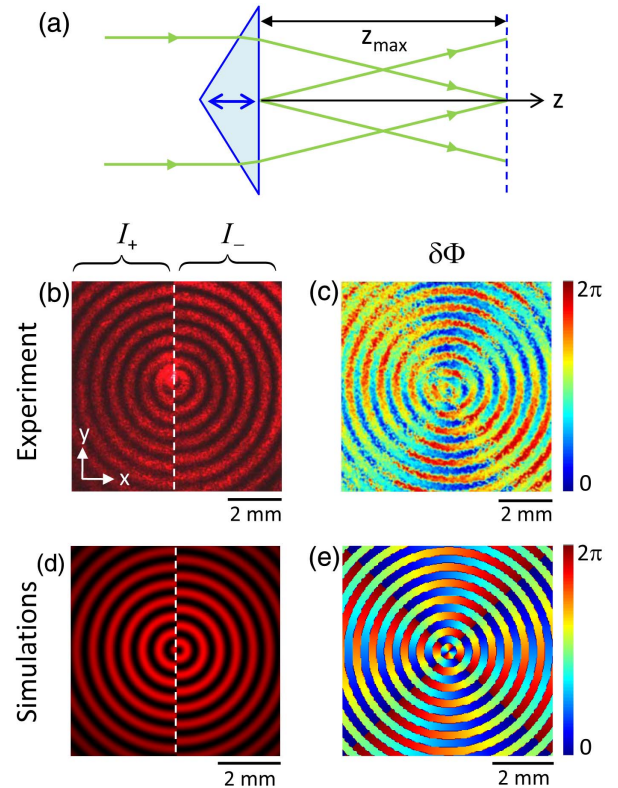


**Fig. 7.** (a) Total intensity near the $z$ axis of a hollow beam with self-imaged orbital angular momentum generated from an incident $\mathbf{c}_+$ Laguerre–Gaussian beam of order $l = -1$. (b) Orbital angular momentum density $M_z(r, z)$ color map, where luminance is proportional to the total intensity shown in panel (a). Transverse phase profiles of the $\mathbf{c}_-$ and $\mathbf{c}_+$ polarized components are shown in (c) and (d), respectively.



**Fig. 8.** (a) Illustration of the experimental approach: the output light field is observed at a distance $z = z_{max}$ from the birefringent axicon for a $\mathbf{c}_+$ polarized incident Gaussian beam. (b) and (d) Juxtaposed transverse intensity distribution $I_\pm$ of the $\mathbf{c}_\pm$ polarized components of the output field at a distance $z_{obs}$ from the axicon above which a central shadow appears. (c) and (e) Corresponding phase difference $\delta\Phi$ between the $\mathbf{c}_\pm$ polarized components. (b) and (c) Experiments. (d) and (e) Simulations. Incident beam waist is $w \simeq 6.5$ mm.

the phase characteristics of SOPHIE are assessed by measuring the spatial distribution of the azimuth angle $\psi$ of the polarization ellipse from the reduced Stokes parameters $s_1$ and $s_2$ following $\psi = (1/2)\arctan(s_2/s_1)$. Indeed, this gives access to the optical phase difference between the $\mathbf{c}_\pm$ components, $\delta\Phi = \Phi_+ - \Phi_-$, from the relationship $\delta\Phi = 2\psi$ [36].

Comparison between observations and predictions can be assessed within a ray-optics description. Indeed, the characteristic diffraction length associated with the highest spatial frequency of the output beam just after the birefringent axicon, which scales as $\Lambda^2/\lambda$, is of the order of 1 m and is typically two decades larger that $z_{max}$. Therefore, one can approximate the field at $z = z_{max}$ as the 1:1 inverted image of the field at $z = 0^+$; see Eq. (8). Results are shown in Figs. 8(d) and 8(e), which exhibit fair agreement.

## 6. DISCUSSION

As mentioned in Section 2.C, we have restricted our approach to paraxial analysis, which is consistent with the magnitude of the involved partial wave tilt angle $\theta$ with respect to the propagation axis. It remains, however, instructive to quantify nonparaxial spin–orbit effects, since they are arguably expected to contribute to SOPHIE of light. First, we notice that nonparaxial spin–orbit contributions refer not only to higher-order corrections of spin–orbit effects due to the material anisotropy, but, indeed, they also arise from mere reflection and refraction of light as reviewed in [37]. More precisely, for moderate angles, the magnitude of the latter contributions scale as $\zeta_\perp = \theta^2/4$ and $\zeta_z = \theta\sqrt{2}$ for the transverse and longitudinal parts of the field, respectively [37].

Regarding the transverse field transformation made by the birefringent axicon [see Eq. (8)], the relevant angle is $\beta$ and gives $\zeta_\perp \simeq 0.01$. This should be compared with the nondiagonal spin–orbit term in Eq. (8), which scales as $\sin(\Delta/2)$, and where $\Delta$ is the birefringent phase retardation arising from the material anisotropy of the uniaxial crystal. Since the periodic field modulation discussed in the present work is related with values of $\Delta$ covering a range that is several times larger than $2\pi$, it is relevant to neglect the nonparaxial spin–orbit contributions overall. On the other hand, longitudinal correction magnitude $\zeta_z = 0.28$ implies the appearance of a vortex in the longitudinal field component of topological charge $l + \sigma$ with intensity corrections ($\propto \zeta_z^2$) of the order of $\lesssim 10\%$. The ensuing consequences should be evaluated by using a $3 \times 3$ matrix field transformation [37], which can be the purpose of a future work.

Summarizing, we demonstrated that homogeneous optically anisotropic crystals can be used as SOPHIE optical elements capable of producing light fields with various kinds of self-imaged properties without a specific wavelength requirement. In particular, we unveiled the realization of periodic bottle beams, corrugated hollow beams, and hollow needle beams with spatially modulated optical angular momentum, from a single incident beam of the Laguerre–Gauss family. Extension to other kinds of paraxial beams (e.g., Hermite–Gauss or Ince–Gauss) is likely to extend the application potential of the proposed self-imaged beam shaping technique, which may find use in optical trapping and manipulation of small-scale objects and soft matter.

## REFERENCES

1. K. Dholakia and T. Čižmár, "Shaping the future of manipulation," Nat. Photon. **5**, 335–342 (2011).
2. M. Woerdemann, C. Alpmann, M. Esseling, and C. Denz, "Advanced optical trapping by complex beam shaping," Laser Photon. Rev. **7**, 839–854 (2013).
3. R. Barboza, U. Bortolozzo, M. G. Clerc, S. Residori, and E. Vidal-Henriquez, "Optical vortex induction via light–matter interaction in liquid-crystal media," Adv. Opt. Photon. **7**, 635–683 (2015).
4. A. Volyar, T. Fadeyeva, and Y. A. Egorov, "Vector singularities of Gaussian beams in uniaxial crystals: optical vortex generation," Tech. Phys. Lett. **28**, 958–961 (2002).
5. A. Volyar and T. Fadeyeva, "Generation of singular beams in uniaxial crystals," Opt. Spectrosc. **94**, 235–244 (2003).
6. A. Ciattoni, G. Cincotti, and C. Palma, "Circularly polarized beams and vortex generation in uniaxial media," J. Opt. Soc. Am. A **20**, 163–171 (2003).
7. T. King, W. Hogervorst, N. Kazak, N. Khilo, and A. Ryzhevich, "Formation of higher-order Bessel light beams in biaxial crystals," Opt. Commun. **187**, 407–414 (2001).
8. N. A. Khilo, E. S. Petrova, and A. A. Ryzhevich, "Transformation of the order of Bessel beams in uniaxial crystals," Quantum Electron. **31**, 85–89 (2001).
9. T. A. Fadeyeva, V. G. Shvedov, Y. V. Izdebskaya, A. V. Volyar, E. Brasselet, D. N. Neshev, A. S. Desyatnikov, W. Krolikowski, and Y. S. Kivshar, "Spatially engineered polarization states and optical vortices in uniaxial crystals," Opt. Express **18**, 10848 (2010).
10. S. Khonina and S. Kharitonov, "Comparative investigation of nonparaxial mode propagation along the axis of uniaxial crystal," J. Mod. Opt. **62**, 125–134 (2015).
11. S. Chavez-Cerda, E. Tepichin, M. A. Meneses-Nava, G. Ramirez, and J. M. Hickmann, "Experimental observation of interfering Bessel beams," Opt. Express **3**, 524–529 (1998).
12. T. Cizmar, V. Garces-Chavez, K. Dholakia, and P. Zemanek, "Optical conveyor belt for delivery of submicron objects," Appl. Phys. Lett. **86**, 174101 (2005).
13. D. McGloin, G. Spalding, H. Melville, W. Sibbett, and K. Dholakia, "Three-dimensional arrays of optical bottle beams," Opt. Commun. **225**, 215–222 (2003).
14. P. Muys, T. Moser, and T. Feurer, "Polarization eigenstates of an axially symmetric laser beam in a c-cut uniaxial crystal," J. Opt. Soc. Am. B **24**, 2627–2631 (2007).
15. E. Wolf, "Electromagnetic diffraction in optical systems. I. An integral representation of the image field," Proc. R. Soc. Lond. A **253**, 349–357 (1959).
16. E. Wolf and Y. Li, "Conditions for the validity of the Debye integral representation of focused fields," Proc. R. Soc. Lond. A **39**, 205–210 (1981).
17. B. Richards and E. Wolf, "Electromagnetic diffraction in optical systems. II. Structure of the image field in an aplanatic system," Proc. R. Soc. Lond. A **253**, 358–379 (1959).
18. C. Loussert and E. Brasselet, "Efficient scalar and vectorial singular beam shaping using homogeneous anisotropic media," Opt. Lett. **35**, 7–9 (2010).
19. E. Brasselet, Y. Izdebskaya, V. Shvedov, A. S. Desyatnikov, W. Krolikowski, and Y. S. Kivshar, "Dynamics of optical spin-orbit coupling in uniaxial crystals," Opt. Lett. **34**, 1021–1023 (2009).
20. D. McGloin and K. Dholakia, "Bessel beams: diffraction in a new light," Contemp. Phys. **46**, 15–28 (2005).
21. J. Arlt and M. J. Padgett, "Generation of a beam with a dark focus surrounded by regions of higher intensity: the optical bottle beam," Opt. Lett. **25**, 191–193 (2000).
22. V. G. Shvedov, Y. V. Izdebskaya, A. V. Rode, A. Desyatnikov, W. Krolikowski, and Y. S. Kivshar, "Generation of optical bottle beams by incoherent white-light vortices," Opt. Express **16**, 20902–20907 (2008).

23. V. G. Shvedov, C. Hnatovsky, N. Shostka, and W. Krolikowski, "Generation of vector bottle beams with a uniaxial crystal," J. Opt. Soc. Am. B **30**, 1–6 (2013).

24. A. Turpin, V. Shvedov, C. Hnatovsky, Y. V. Loiko, J. Mompart, and W. Krolikowski, "Optical vault: a reconfigurable bottle beam based on conical refraction of light," Opt. Express **21**, 26335–26340 (2013).

25. Y. V. Loiko, A. Turpin, T. K. Kalkandjiev, E. U. Rafailov, and J. Mompart, "Generating a three-dimensional dark focus from a single conically refracted light beam," Opt. Lett. **38**, 4648–4651 (2013).

26. J. Arlt, V. Garces-Chavez, W. Sibbett, and K. Dholakia, "Optical micromanipulation using a Bessel light beam," Opt. Commun. **197**, 239–245 (2001).

27. V. Garces-Chavez, D. McGloin, H. Melville, W. Sibbett, and K. Dholakia, "Simultaneous micromanipulation in multiple planes using a self-reconstructing light beam," Nature **419**, 145–147 (2002).

28. V. G. Shvedov, A. S. Desyatnikov, A. V. Rode, W. Krolikowski, and Y. S. Kivshar, "Optical guiding of absorbing nanoclusters in air," Opt. Express **17**, 5743–5757 (2009).

29. A. S. Desyatnikov, V. G. Shvedov, A. V. Rode, W. Krolikowski, and Y. S. Kivshar, "Photophoretic manipulation of absorbing aerosol particles with vortex beams: theory versus experiment," Opt. Express **17**, 8201–8211 (2009).

30. J. Arlt, K. Dholakia, J. Soneson, and E. M. Wright, "Optical dipole traps and atomic waveguides based on Bessel light beams," Opt. Commun. **63**, 063602 (2001).

31. M. S. Soskin, V. N. Gorshkov, M. V. Vasnetsov, J. T. Malos, and N. R. Heckenberg, "Topological charge and angular momentum of light beams carrying optical vortices," Phys. Rev. A **56**, 4064–4075 (1997).

32. D. G. Grier, "A revolution in optical manipulation," Nature **424**, 810–816 (2003).

33. N. B. Simpson, K. Dholakia, L. Allen, and M. J. Padgett, "Mechanical equivalence of spin and orbital angular momentum of light: an optical spanner," Opt. Lett. **22**, 52–54 (1997).

34. J. Guck, R. Ananthakrishnan, H. Mahmood, T. J. Moon, C. C. Cunningham, and J. Kas, "The optical stretcher: a novel laser tool to micromanipulate cells," Biophys. J. **81**, 767–784 (2001).

35. J. Xavier, R. Dasgupta, S. Ahlawat, J. Joseph, and P. K. Gupta, "Three dimensional optical twisters-driven helically stacked multi-layered microrotors," Appl. Phys. Lett. **100**, 121101 (2012).

36. E. Brasselet, N. Murazawa, H. Misawa, and S. Juodkazis, "Optical vortices from liquid crystal droplets," Phys. Rev. Lett. **103**, 103903 (2009).

37. K. Y. Bliokh, E. A. Ostrovskaya, M. A. Alonso, O. G. Rodríguez-Herrera, D. Lara, and C. Dainty, "Spin-to-orbital angular momentum conversion in focusing, scattering, and imaging systems," Opt. Express **19**, 26132–26149 (2011).